A hierarchical model for rate-dependent polycrystals

Sivasambu Mahesh [a]

[a] *Departments of Mechanical and Aerospace Engineering, Indian Institute of Technology, Kanpur 208016. India.*

Abstract

A hierarchical model of a polycrystalline aggregate of rigid viscoplastic grains is formulated, and a robust and efficient computational algorithm for its solution is proposed. The polycrystalline aggregate is modeled as a binary tree. The leaves of the binary tree represent grains, and higher tree nodes represent increasingly larger sub-aggregates of grains. The root of the tree represents the entire polycrystalline aggregate. Velocity and traction continuity are enforced across the interface between the children of each non-leaf node in the binary tree. The hierarchical model explicitly models intergranular interactions but is nevertheless comparable in computational effort to the mean-field models of polycrystal plasticity. Simulations of tensile, compressive, torsional, and plane strain deformation of copper lead to predictions in good agreement with experiments, and highlight the interconnection between grain deformations and intergranular constraints. It is inferred from the results that a hybrid mean-field/hierarchical model represents a computationally efficient methodology to simulate polycrystal deformation while accounting for intergranular interactions.

Key words: Crystal plasticity, Hierarchical model, Texture modeling, Numerical Algorithms

1 Introduction

Models presently available for predicting the mechanical response of a polycrystalline aggregate to imposed load or deformation may broadly be categorized either as mean field models, or as microstructural models. The simplest mean field model, due to Taylor (1938), suffices to qualitatively explain the macroscopic mechanical response and texture evolution during monotonic homogeneous deformation in high symmetry materials (Hirsch and Lucke, 1988a,b, Tomé et al., 1984), despite neglecting all intergranular interactions. The self consistent model, another mean field model developed by Hill (1965), Molinari et al. (1987), and Lebensohn and Tomé (1993) treats intergranular interactions in an average sense by requiring each grain to deform compatibly with a homogeneous effective medium representing the polycrystal. Mean field models neither account for the topology of grain and phase arrangement, nor demand intergranular compatibility across grain boundaries.

On the other hand, microstructural models can account for the microstructure in detail. The earliest microstructural model, due to Lin (1964), regarded the polycrystal as a planar periodic tiling of square grains, and imposed displacement compatibility, and traction continuity along the edges of each square. More recently, the crystal plasticity based finite element method of Kalidindi et al. (1992) has been widely applied (Grujicic et al., 2003, Manonukul and Dunne, 2004, Héripré et al., 2007) to model the details of the microstructure and intergranular interactions in order to explain experimentally observed microstructural phenomena in polycrystals. Buchheit et al. (2005) have discussed

the strengths and shortcomings of such models. An alternative, the N-site model due to Lebensohn (2001) can also include the details of the microstructure into the model, and is perhaps the computationally fastest method of this class.

Intergranular interactions are important in modeling the evolution of the grain sub-structure, which sensitively depends upon the constraints imposed upon a grain by its neighbors (Leffers and Christoffersen, 1997, Butler and McDowell, 1998, Thorning et al., 2005). Much recent work has focused on substructure/microstructure sensitive modeling of the plastic response of a variety of crystalline materials, under a range of loading paths and deformation conditions, e.g., (Peeters et al., 2001a,b, Mahesh et al., 2004, Mayeur and McDowell, 2007, Beyerlein and Tomé, 2008, Shenoy et al., 2008, Shiekhelsouk et al., 2008) Also, intergranular interactions must be accounted for in modeling the nucleation and propagation of instabilities in a polycrystal (Dillamore and Katoh, 1974, Barnett et al., 2004, Paul et al., 2007), in modeling the response of polycrystals with fine or elongated grains (Gan et al., 2007, Lee et al., 2007), or where the test coupon is in the form of a thin membrane (Nemat-Nasser et al., 2006). In each of these cases the deformation of a grain may be significantly influenced by that of its neighbors (Hughes et al., 1997). Evidently, modeling those phenomena that hinge upon intergranular interactions lies beyond the scope of the mean field models, and falls within the purview of the microstructural models.

The shortcoming of the microstructural models is that they are at least two orders of magnitude more computationally intensive than the mean field models. This is especially significant because it is presently computationally prohibitive to incorporate the plastic response of a material point calculated from

a microstructural model to inform a larger simulation of a non-homogeneous deformation process such as those in the studies of Guan et al. (2006), Zamiri et al. (2007), Wu et al. (2007), Duchêne et al. (2007), or even to use it to synthesize a texture dependent yield locus database (Knezevic et al., 2008). Therefore, in situations that call for consideration of intergranular interactions, but where only the statistics, and not the exact details of the microstructure are significant, it is clearly advantageous to coarse-grain the intergranular interaction and thus reduce the computational effort involved in solving the model.

Strategies for coarse-graining the intergranular interactions have received much attention recently. The LAMEL model of Van Houtte et al. (2002) accounts for intergranular interactions in a polycrystal by imposing the applied rolling deformation upon pairs of rate-independent grains deforming compatibly across an intergranular interface parallel to the rolling plane. Van Houtte et al's (Van Houtte et al., 2005) ALAMEL model additionally imposes approximate traction continuity between the interacting grains assuming a zone of continuous traction variation between interacting grains. We also note here the numerous works that have invoked similar considerations in order to model the compatible interaction between sub-structural features within a grain. Velocity and traction continuity was used by Lebensohn (1999) and by Proust et al. (2007) to model the interaction between the matrix and twin bands within a grain in the context of deformation twinning studies using a self-consistent model. Whereas Lebensohn (1999) and Proust et al. (2007) only model interactions between pairs of sub-grain structures by forbidding their matrix and twin bands from dividing further, Ortiz and Repetto (1999), and Ortiz et al. (2000) have used the hierarchical framework to model the formation of

nested deformation bands of arbitrary depth within the context of minimizing a non-convex plastic work function.

In this work, we model a rate-dependent polycrystalline aggregate as a hierarchical arrangement of interacting sub-aggregates. Velocity and traction continuity between sub-aggregates is enforced at each level of the hierarchy. The model formulation allows several common constraints (full, and relaxed constraints, self-consistent constraints, etc.) to be imposed upon the root node of the hierarchy. We begin by formulating the model for arbitrary hierarchies in Sec. 2.1–2.3 and in Sec. 2.4, detail a novel, robust and efficient computational algorithm to solve the system of non-linear equations that result from the formulation. Then in Sec. 3, we apply the hierarchical model to simulation monotonic deformation of a copper polycrystal along various load paths, and compare the predictions with experiments, and with those of the Taylor and self-consistent mean field models.

2 The Hierarchical Polycrystal Model

2.1 Governing equations

Consider a polycrystalline aggregate of N_g rigid-viscoplastic rate dependent grains, each of which obeys the following constitutive relation between the isochoric strain rate ($\dot{\boldsymbol{\epsilon}}$) and deviatoric stress ($\boldsymbol{\sigma}$), both assumed uniform over the domain of the grain (Asaro and Needleman, 1985, Canova et al., 1988):

$$\dot{\boldsymbol{\epsilon}} = \sum_{s=1}^{S} \boldsymbol{m}^s \left| \frac{\boldsymbol{\sigma} : \boldsymbol{m}^s}{\tau^s} \right|^n \operatorname{sign}(\boldsymbol{\sigma} : \boldsymbol{m}^s), \tag{1}$$

where, $\boldsymbol{m}^s = (\boldsymbol{n}^s \otimes \boldsymbol{b}^s + \boldsymbol{b}^s \otimes \boldsymbol{n}^s)/2$, $s = 1, \ldots, S$ denotes the Schmid tensor of the s-th slip system with unit normal $\boldsymbol{n}^s$ and unit Burgers vector $\boldsymbol{b}^s$, τ^s denotes the critical resolved shear stress of slip system s, and n denotes the reciprocal rate sensitivity. $\dot{\gamma}^s = |\boldsymbol{\sigma} : \boldsymbol{m}^s/\tau^s|^n \text{sign}(\boldsymbol{\sigma} : \boldsymbol{m}^s)$ is the slip rate of slip system s.

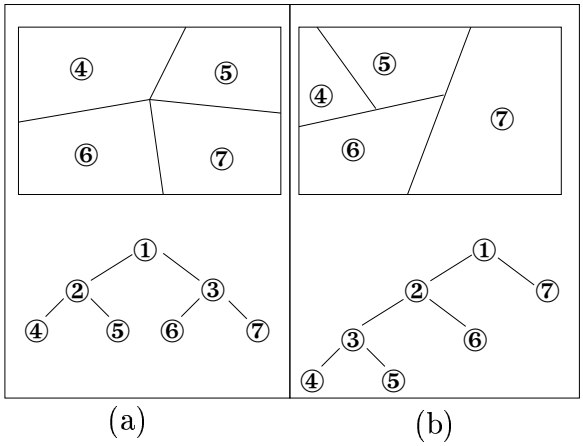

Fig. 1. Schematic drawings of two grain placement schemes for $N_g = 4$ grains in the microstructure (first row), and the binary trees corresponding to them (second row). In both cases, node 1 is the root of the tree, and nodes 4, 5, 6, and 7 are the leaves of the tree denoting grains. The compatibility conditions between the nodes of the tree are however markedly different in case (a) and case (b).

We model the polycrystalline aggregate as a binary tree. Following standard nomenclature (Cormen et al., 1990), each node k of the binary tree will be assigned two child nodes denoted as $l(k)$ and $r(k)$, and a parent node $p(k)$. Nodes $l(k)$ and $r(k)$ are said to be siblings of each other, and we will use the notation $s(l(k)) = r(k)$, and $s(r(k)) = l(k)$. If neither $l(k)$ nor $r(k)$ exist, k is called a leaf of the tree. Likewise, if $p(k)$ does not exist, k is called the root of the tree.

Two schematic examples of the microstructure, and the corresponding binary trees are shown in Fig. 1. Each of the N_g grains in the polycrystal is identified

with a leaf of the tree. With no loss of generality in representing the physical connectivity between grains in a polycrystal, nodes that have only one child are disallowed from our binary tree. Then, it can be seen that if N_g is the number of leaves, the number of nodes in the tree must be $N_n = 2N_g - 1$. Higher nodes representing increasingly larger sub-aggregates of grains are assigned a volume fraction $w^{[k]}$ such that for all k, $w^{[k]} = w^{[l(k)]} + w^{[r(k)]}$. The volume fraction of the leaves is an input to the model say, from a texture description of the microstructure. We also define $\rho^{[k]} = w^{[l(k)]}/w^{[k]} \in [0, 1]$, so that $w^{[r(k)]}/w^{[k]} = 1 - \rho^{[k]}$. The highest node of the binary tree, the root, represents the entire polycrystalline aggregate. We will presently consider the formulation and solution of the system of equations of a polycrystalline aggregate represented by a binary tree. A discussion of the best representation of a given microstructure by a binary tree will be postponed to Sec. 4.

We begin the formulation by defining the deviatoric stress $\boldsymbol{\sigma}$ and the isochoric strain rate $\dot{\boldsymbol{\epsilon}}$ at each non-leaf node k as the volume fraction weighted averages of those of its children:

$$\begin{aligned} \boldsymbol{\sigma}^{[k]} =& \rho^{[k]}\boldsymbol{\sigma}^{[l(k)]} + (1-\rho^{[k]})\boldsymbol{\sigma}^{[r(k)]}, \\ \dot{\boldsymbol{\epsilon}}^{[k]} =& \rho^{[k]}\dot{\boldsymbol{\epsilon}}^{[l(k)]} + (1-\rho^{[k]})\dot{\boldsymbol{\epsilon}}^{[r(k)]}. \end{aligned} \tag{2}$$

Secondly, deformation compatibility and traction continuity is demanded between siblings $l(k)$ and $r(k)$ as follows: If the interfacial normal between $l(k)$ and $r(k)$ is $\boldsymbol{\nu}^{[k]}$, and the velocity gradient in node k is $\boldsymbol{L}^{[k]}$, we will require that

$$\begin{aligned} [\![\boldsymbol{L}^{[k]}]\!] = \boldsymbol{L}^{[r(k)]} - \boldsymbol{L}^{[l(k)]} = \boldsymbol{\lambda}^{[k]} \otimes \boldsymbol{\nu}^{[k]}, \\ \boldsymbol{\sigma}^{[r(k)]}\boldsymbol{\nu}^{[k]} = \boldsymbol{\sigma}^{[l(k)]}\boldsymbol{\nu}^{[k]}, \end{aligned} \tag{3}$$

for some $\boldsymbol{\lambda}^{[k]}$ (Hill, 1961). A necessary condition (Mahesh, 2005) for Eq. (3a)

to be satisfied is that

$$[\![\dot{\boldsymbol{\epsilon}}]\!]^{[k]} = \dot{\boldsymbol{\epsilon}}^{[r(k)]} - \dot{\boldsymbol{\epsilon}}^{[l(k)]} = (\boldsymbol{\lambda}^{[k]} \otimes \boldsymbol{\nu}^{[k]} + \boldsymbol{\nu}^{[k]} \otimes \boldsymbol{\lambda}^{[k]})/2, \tag{4}$$

in which case, $\boldsymbol{\lambda}^{[k]} = 2[\![\dot{\boldsymbol{\epsilon}}]\!]^{[k]}\boldsymbol{\nu}^{[k]} - ([\![\dot{\boldsymbol{\epsilon}}]\!]^{[k]}\boldsymbol{\nu}^{[k]} \cdot \boldsymbol{\nu}^{[k]})\boldsymbol{\nu}^{[k]}$. Eq. (4) serves to enforce the symmetric part of Eq. (3a). The anti-symmetric part of Eq. (3a) is satisfied by imposing lattice spins $\boldsymbol{W}_{\text{lat}}^{[k]}$ to the children of node k. To this end, we decompose the velocity gradient of the k-th node as (Mahesh, 2005)

$$\boldsymbol{L}^{[k]} = \boldsymbol{L}_{\text{ss}}^{[k]} + \boldsymbol{W}_{\text{lat}}^{[k]}, \tag{5}$$

where,

$$\boldsymbol{L}_{\text{ss}}^{[k]} = \begin{cases} \sum_s \dot{\gamma}^{s,[k]} \boldsymbol{b}^{s,[k]} \otimes \boldsymbol{n}^{s,[k]}, & \text{if } k \in \mathscr{L}, \text{ and} \\ \langle \boldsymbol{L}_{\text{ss}}^{[k]} \rangle = \rho^{[k]} \boldsymbol{L}_{\text{ss}}^{[l(k)]} + (1-\rho^{[k]}) \boldsymbol{L}_{\text{ss}}^{[r(k)]}, & \text{if } k \notin \mathscr{L}, \end{cases} \tag{6}$$

where $\mathscr{L}$ denotes the set of all the leaves of the binary tree. In this work, $\boldsymbol{L}_{\text{ss}}^{[k]}$ will quantify the deformation of node k due to slip only. Compatibility of deformation between the children of node k is obtained by setting (Mahesh, 2005)

$$\begin{aligned} \boldsymbol{W}_{\text{lat}}^{[l(k)]} &= \text{skew}\left\{ (\boldsymbol{L}^{[k]} - \langle \boldsymbol{L}_{\text{ss}}^{[k]} \rangle) - (1-\rho^{[k]})(\boldsymbol{\lambda}^{[k]} \otimes \boldsymbol{\nu}^{[k]} - [\![\boldsymbol{L}_{\text{ss}}^{[k]}]\!]) \right\}, \\ \boldsymbol{W}_{\text{lat}}^{[r(k)]} &= \text{skew}\left\{ (\boldsymbol{L}^{[k]} - \langle \boldsymbol{L}_{\text{ss}}^{[k]} \rangle) + \rho^{[k]}(\boldsymbol{\lambda}^{[k]} \otimes \boldsymbol{\nu}^{[k]} - [\![\boldsymbol{L}_{\text{ss}}^{[k]}]\!]) \right\}. \end{aligned} \tag{7}$$

The problem of determining consistent fields in the hierarchical polycrystal thus amounts to finding the five independent components of deviatoric stress $\boldsymbol{\sigma}^{[k]}$, $k \in \mathscr{L}$ at the N_g leaves such that Eq. (3b) (2 equations) and Eq. (4) (3 equations) are satisfied at each of the $N_n - N_g = N_g - 1$ non-leaf nodes of the binary tree. This results in $5(N_g - 1)$ non-linear algebraic equations, which, for their closure require the imposition of five boundary conditions. The system of non-linear algebraic equations is dense because every leaf (grain) shares an

ancestor in the hierarchy with every other leaf. Intractably large matrices may result if the standard methodology (Powell, 1970) for the solution of non-linear equations were used. Note that the intrinsically banded structure of the finite element method is not available for the present hierarchical structure of the problem. The hierarchical nature of the present problem however lends itself to a different strategy for an efficient piecemeal solution, as detailed below.

2.2 State evolution of the polycrystal

Once $\boldsymbol{\sigma}^{[k]}$ and $\dot{\boldsymbol{\epsilon}}^{[k]}$ conforming to Eqs. (2), (3b), and (4) at each node k are determined, the lattice spins $\boldsymbol{W}_{\text{lat}}^{[k]}$ at each node k are determined from Eq. (7), and used to update the lattice orientations of the grains. The shape of node k, quantified by its deformation gradient tensor $\boldsymbol{F}^{[k]}$ can also be updated using (Kocks et al., 1998)

$$\dot{\boldsymbol{F}}^{[k]} = \boldsymbol{L}^{[k]}\boldsymbol{F}^{[k]}. \tag{8}$$

The orientation of the interfacial normal between the children of node k, is assumed to evolve with the shape of node k: If the interfacial normal were $\boldsymbol{\nu}_0^{[k]}$ when the deformation gradient of node k is $\boldsymbol{F}_0^{[k]}$, the interfacial normal is taken as (Mahesh and Tomé, 2004)

$$\boldsymbol{\nu}^{[k]} = \boldsymbol{F}_0^{[k]^T}\boldsymbol{F}^{[k]^{-1}}\boldsymbol{\nu}_0^{[k]} / \| \boldsymbol{F}_0^{[k]^T}\boldsymbol{F}^{[k]^{-1}}\boldsymbol{\nu}_0^{[k]} \|, \tag{9}$$

after the evolution of the deformation gradient to $\boldsymbol{F}^{[k]}$.

The hardening law used in the present study is of the extended Voce type given by Tomé et al. (1984)

$$\tau(\Gamma) = \tau_0 + (\tau_1 + \theta_1 \Gamma)\left[1 - \exp(-\Gamma\theta_0/\tau_1)\right], \tag{10}$$

where Γ denotes the shear strain accumulated in all the slip systems of the grain. Increment of the critical resolved shear stress τ^s in slip system s follows Kocks et al. (1998)

$$\dot{\tau}^s = \frac{d\tau(\Gamma)}{d\Gamma} \sum_{s'} H^{ss'} \dot{\gamma}^{s'}, \tag{11}$$

where the summation is over all the slip systems indexed by s', $\underline{H}$ denotes the 12×12 hardening matrix, and $d\tau(\Gamma)/d\Gamma$ is obtained by differentiating Eq. (10).

$\underline{H}$ used in this work incorporates the experimental observation of Franciosi and Zaoui (1982) that latent hardening of slip systems in copper is anisotropic and depends on the type of interaction between dislocations in the active and latent slip systems. The value of $H_{ss'}$, $s, s' \in \{1, \ldots, 12\}$ is chosen depending upon whether the interaction between s and s' is of the self hardening (h_0), coplanar (h_1), colinear (h_1), Hirth locking (h_1), glissile junction forming (h_2), or Lomer-Cottrell junction forming (h_3) types. According to Franciosi and Zaoui (1982) and Pierce et al. (1982), $1 \leq h_0 \leq h_1 \leq h_2 \leq h_3 \leq 1.4$ in copper.

The hardening model described above is a modification of models available in the literature. Surveys of hardening models may be found in Weng (1987) (parametric models), and Mahesh et al. (2004) (sub-structural models). As an example of an alternative definition of latent hardening coefficients, Weng

(1987) has suggested

$$h_{ss'} = \alpha_1 + (1 - \alpha_1)\cos\theta_{ss'}\cos\phi_{ss'} + \alpha_2 \sin\theta_{ss'} + \alpha_3 \sin\phi_{ss'}, \qquad (12)$$

where $\alpha_{(.)}$ are fitting parameters in place of $h_{(.)}$ in the present model, and $\theta_{ss'}$ is the angle between the slip directions the s-th and s'-th slip systems, and $\phi_{ss'}$ is the angle between their slip plane normals. Weng (1987) observes that hardening matrices of this form can accommodate several types of hardening including, isotropic and kinematic hardening. This observation also applies to the hardening matrix $\underline{H}$ used in this work.

2.4 Solution methodology for the hierarchical model

Prior to detailing an algorithm for the solution of the $5N_g$ deviatoric stress components satisfying Eq. (3b), Eq. (4), and the imposed boundary conditions in Sec. 2.4.8, we set forth key concepts used in the solution.

2.4.1 Continuity conditions in Leibfried-Breuer notation

We refer to Lebensohn et al. (1998) for a description of the 5-dimensional Leibfried-Breuer vector representation of a traceless symmetric matrices whereby the matrix representation of the strain rate and deviatoric stress in the sample coordinate system are $[\dot{\boldsymbol{\epsilon}}] = \sum_{\lambda=1}^{5} \dot{\epsilon}^{(\lambda)} \underline{b}^{(\lambda)}$, and $[\boldsymbol{\sigma}] = \sum_{\lambda=1}^{5} \sigma^{(\lambda)} \underline{b}^{(\lambda)}$, respectively. Here $\underline{b}^{(\lambda)}$ represent symmetric basis matrices that obey the orthonormality condition $\underline{b}^{(\lambda)} : \underline{b}^{(\mu)} = \delta_{\lambda\mu}$. It is easily shown that for a coordinate transformation specified by $[\dot{\boldsymbol{\epsilon}}'] = [\boldsymbol{R}]^T[\dot{\boldsymbol{\epsilon}}][\boldsymbol{R}]$ and $[\boldsymbol{\sigma}'] = [\boldsymbol{R}]^T[\boldsymbol{\sigma}][\boldsymbol{R}]$ where $[\boldsymbol{R}]$ is orthonormal, there exists an orthonormal matrix $\underline{\alpha}$, $\alpha_{\lambda\mu} = [\boldsymbol{R}]^T \underline{b}^{(\mu)} [\boldsymbol{R}] : \underline{b}^{(\lambda)}$ such that $\dot{\epsilon}^{(\lambda)\prime} = \alpha_{\lambda\mu}\dot{\epsilon}^{(\mu)}$, and $\sigma^{(\lambda)\prime} = \alpha_{\lambda\mu}\sigma^{(\mu)}$. Note that $[\cdot]$ denotes the matrix

representation of a tensor in the sample coordinate system, and $\underline{\cdot}$ denotes a matrix.

Let $\underline{\alpha}^{[k]}$ denote the rotation matrix in the Leibfried-Breuer space that corresponds to a physical rotation $\boldsymbol{R}$ from the sample coordinate system to a coordinate system whose 2-axis coincides with the interface normal between the child nodes of node k. Thus the 1 and 3 axes of the interfacial coordinate system will lie in the interface; their actual orientation within the interface is irrelevant. Then, in the Leibfried-Breuer notation, Eq. (3b) and Eq. (4) take the form

$$\underline{P\alpha}^{[k]}[[\dot{\boldsymbol{\epsilon}}^{[k]}]] + \underline{Q\alpha}^{[k]}[[\boldsymbol{\sigma}^{[k]}]] = \underline{0}, \tag{13}$$

where,

$$\underline{P} = \mathrm{diag}(1,1,0,1,0), \quad \text{and} \quad \underline{Q} = \mathrm{diag}(0,0,1,0,1). \tag{14}$$

Eq. (13) is the statement of strain-rate compatibility and traction continuity between the children of node k in Leibfried-Breuer form, and is related to the condition used by Lebensohn (1999) in that his $\underline{K}$ is our $\underline{Q^{-1}P}$. The present treatment however obviates Lebensohn's numerical treatment of infinities.

2.4.2 Boundary conditions in Leibfried-Breuer notation

The boundary conditions imposed upon the root node r of the hierarchy can be specified in the form:

$$\underline{S}[\dot{\boldsymbol{\epsilon}}^{[r]}] + \underline{T}[\boldsymbol{\sigma}^{[r]}] + \underline{U} = \underline{0}. \tag{15}$$

The full constraints (FC) imposition of a strain-rate $\dot{\boldsymbol{\epsilon}}^{\mathrm{imp}}$ at node r is accomplished by setting $\underline{S} = \mathrm{diag}(1,1,1,1,1)$, $\underline{T} = \mathrm{diag}(0,0,0,0,0)$, and $\underline{U} = -\dot{\boldsymbol{\epsilon}}^{\mathrm{imp}}$. Relaxation of constraints (Honeff and Mecking, 1978) on planes perpendicular to the '2'-axis, i.e., $\sigma_{12} = \sigma_{21} = \sigma_{23} = \sigma_{23} = 0$, is accomplished by setting

$\underline{S} = \text{diag}(1,1,0,1,0)$, $\underline{T} = \text{diag}(0,0,1,0,1)$, and $\underline{U} = -(\dot{\epsilon}_1^{\text{imp}}, \dot{\epsilon}_2^{\text{imp}}, 0, \dot{\epsilon}_4^{\text{imp}}, 0)$, where $\dot{\epsilon}_i^{\text{imp}}$ is the i-th Leibfried-Breuer component of the imposed strain rate vector. The interaction equation (Lebensohn and Tomé, 1993, Eq. 18) of the self-consistent method

$$\dot{\boldsymbol{\epsilon}} - \dot{\boldsymbol{E}} = -\tilde{\boldsymbol{M}}(\boldsymbol{\sigma} - \boldsymbol{\Sigma}),$$

where $(\dot{\boldsymbol{\epsilon}}, \boldsymbol{\sigma})$ and $(\dot{\boldsymbol{E}}, \boldsymbol{\Sigma})$ are the strain rate and the deviatoric stress in a grain, and in the homogeneous effective medium, respectively, and $\tilde{\boldsymbol{M}}$ is the interaction matrix, can also be cast in the form of Eq. (15), by setting $\underline{S} = \text{diag}(1,1,1,1,1)$, $\underline{T} = [\tilde{\boldsymbol{M}}]$, and $\underline{U} = [-\dot{\boldsymbol{E}} - \tilde{\boldsymbol{M}}\boldsymbol{\Sigma}]$.

The constraint imposed upon a sub-hierarchy rooted at some non-root node k, $k \neq r$ can also be expressed in form of Eq. (15), by selecting

$$\begin{aligned} \underline{S} &= \underline{P\alpha}^{[p(k)]}, \\ \underline{T} &= \underline{Q\alpha}^{[p(k)]}, \text{ and} \\ \underline{U} &= -(\underline{P\alpha}^{[p(k)]}[\dot{\boldsymbol{\epsilon}}^{[s(k)]}] + \underline{Q\alpha}^{[p(k)]}[\boldsymbol{\sigma}^{[s(k)]}]). \end{aligned} \tag{16}$$

2.4.3 Tangent modulus

We will now derive the tangent modulus of node k, denoted $\boldsymbol{M}^{\text{tg}}[k] = d\dot{\boldsymbol{\epsilon}}^{[k]}/d\boldsymbol{\sigma}^{[k]}$. If node k is a leaf of the hierarchy, its $\boldsymbol{M}^{\text{tg}}[k]$ may be directly computed by differentiating Eq. (1) as shown by Kocks et al. (1998). The calculation below pertains to a non-leaf node k of the hierarchy, and assumes that $\boldsymbol{M}^{\text{tg}}[l(k)]$ and $\boldsymbol{M}^{\text{tg}}[r(k)]$ are known. It is desired to determine the differential change $d\dot{\boldsymbol{\epsilon}}^{[k]}$ given the differential deviatoric stress increment $d\boldsymbol{\sigma}^{[k]}$ subject to the constraints

$$\begin{aligned} d\left(\underline{P\alpha}^{[p(k)]}[\dot{\boldsymbol{\epsilon}}^{[k]}] + \underline{Q\alpha}^{[p(k)]}[\boldsymbol{\sigma}^{[k]}]\right) &= \mathbf{0}, \\ d\left(\underline{P\alpha}^{[k]}[[\![\dot{\boldsymbol{\epsilon}}^{[k]}]\!]] + \underline{Q\alpha}^{[k]}[[\![\boldsymbol{\sigma}^{[k]}]\!]]\right) &= \mathbf{0}. \end{aligned} \tag{17}$$

Eqs. (17) demand preservation of the constraints imposed upon node k by the rest of the hierarchy, and the state of incompatibility between the children of node k to first order, respectively. Following Lebensohn's (Lebensohn, 1999) analysis, we obtain

$$\boldsymbol{M}^{\mathrm{tg}}[k] = \left(\rho^{[k]}\boldsymbol{M}^{\mathrm{tg}}[l(k)]\boldsymbol{A}^{[k]} + (1-\rho^{[k]})\boldsymbol{M}^{\mathrm{tg}}[r(k)]\right)\left(\rho^{[k]}\boldsymbol{A}^{[k]} + (1-\rho^{[k]})\boldsymbol{I}\right)^{-1}, \tag{18}$$

where

$$\boldsymbol{A}^{[k]} = \frac{d\boldsymbol{\sigma}^{[l(k)]}}{d\boldsymbol{\sigma}^{[r(k)]}} = (\underline{P\alpha}^{[k]}\boldsymbol{M}^{\mathrm{tg}}[l(k)] + \underline{Q\alpha}^{[k]})^{-1}(\underline{P\alpha}^{[k]}\boldsymbol{M}^{\mathrm{tg}}[r(k)] + \underline{Q\alpha}^{[k]}). \tag{19}$$

2.4.4 Binary tree related definitions and notation

The height of node k, $h[k]$, in the hierarchy is defined as:

$$h[k] = \begin{cases} 1, & \text{if } k \in \mathscr{L}, \\ 1 + \max(h[l(k)], h[r(k)]), & \text{if } k \notin \mathscr{L}. \end{cases}$$

The set of nodes of height $\hbar$ in the binary tree will be denoted by $\mathscr{H}^{\hbar}$. The set of descendants of node k, denoted as $\mathscr{D}[k]$ is defined as

$$\mathscr{D}[k] = \begin{cases} \{k\}, & \text{if } l(k) \text{ and } r(k) \text{ do not exist}, \\ \{k, \mathscr{D}[l(k)], \mathscr{D}[r(k)]\}, & \text{otherwise}. \end{cases}$$

The distance, $d(k,l)$ between node k, and node $l \in \mathscr{D}[k]$ is defined as

$$d(k,l) = \begin{cases} 0, & \text{if } k = l \text{ and}, \\ 1 + d(k, p(l)), & \text{otherwise}. \end{cases}$$

The set of all descendants of node k, within a distance b is denoted by $\mathscr{D}^b[k] \subseteq \mathscr{D}[k]$. The set of nodes $l \in \mathscr{D}^b[k]$ that are either distant b from k, or are leaves

of the hierarchy, will be denoted as $\mathscr{L}^b[k]$. In Fig. 1(b), $\mathscr{D}^3[1] = \{1, 2, 3, 6, 7\}$, $\mathscr{L}^3[1] = \{3, 6, 7\}$, $\mathscr{D}^3[2] = \{2, 3, 4, 5, 6\}$, and $\mathscr{L}^3[2] = \{4, 5, 6\}$.

2.4.5 Measure of incompatibility

For integral b (chosen according to computer memory constraints), we define the incompatibility below node k as

$$e^b[k] = \left\{ \left\| \underline{I}^{[k]} \right\|^2 + \sum_{l \in \mathscr{D}^b[k]} \left\| \underline{P\alpha}^{[l]} [[\dot{\boldsymbol{\epsilon}}^{[l]}]] + \underline{Q\alpha}^{[l]} [[\boldsymbol{\sigma}^{[l]}]] \right\|^2 \right\}^{1/2}, \tag{20}$$

where the 2-norm is understood, and where,

$$\underline{I}^{[k]} = \begin{cases} \underline{P\alpha}^{[p(k)]} [[\dot{\boldsymbol{\epsilon}}^{[p(k)]}]] + \underline{Q\alpha}^{[p(k)]} [[\boldsymbol{\sigma}^{[p(k)]}]], & \text{if } k \neq r \text{ and,} \\ \underline{S}[\dot{\boldsymbol{\epsilon}}^{[k]}] + \underline{T}[\boldsymbol{\sigma}^{[k]}] + \underline{U}, & \text{if } k = r. \end{cases} \tag{21}$$

$\underline{I}^{[k]}$ quantifies the incompatibility between the root of the sub-hierarchy $\mathscr{D}^b[k]$, and the rest of the hierarchy if the sub-hierarchy is rooted at an internal node of the binary tree; otherwise it quantifies the incompatibility of the fields in node k with the imposed deformation. The second term in Eq. (20) quantifies the residue in Eq. (13) within a block of height b rooted at node k.

2.4.6 Linearized continuity conditions

Using Eq. (2), $e^b[k]$ can be expressed as $e^b[k] = \|\underline{F}^b[k]\|^2$, where

$$\underline{F}^b[k] = \underline{A}^b[k] \underline{\dot{E}}^b[k] + \underline{B}^b[k] \underline{\Sigma}^b[k] + \underline{C}[k], \tag{22}$$

and $\underline{\dot{E}}^b[k] = (\dot{\boldsymbol{\epsilon}}^{l_1}, \dot{\boldsymbol{\epsilon}}^{l_1}, \ldots, \dot{\boldsymbol{\epsilon}}^{l_p})^T$, $\underline{\Sigma}^b[k] = (\boldsymbol{\sigma}^{l_1}, \boldsymbol{\sigma}^{l_2}, \ldots, \boldsymbol{\sigma}^{l_p})^T$, and $\{l_1, l_2, \ldots, l_p\} = \mathscr{L}^b[k]$. The coefficient matrices $\underline{A}^b[k]$ and $\underline{B}^b[k]$ are formed by volume fraction weighted summation of $\underline{P\alpha}^{[l]}$ and $\underline{Q\alpha}^{[l]}$, $l \in \mathscr{D}^b[k]$ and the loading vector $\underline{C}[k]$

is formed from $\underline{I}^{[k]}$. The non-linearity of $\underline{F}^b[k]$ arises from the relationship between $\dot{\underline{E}}^b[k]$, and $\underline{\Sigma}^b[k]$ in Eq. (1). For the purpose of finding a perturbation $\delta\underline{\Sigma}^b[k]$ that reduces $\|\underline{F}^b[k]\|$, we define the Jacobian of $\underline{F}^b[k]$ as

$$\underline{J}^b[k] = \partial\underline{F}^b[k]/\partial\underline{\Sigma}^b[k] = (\underline{A}^b[k][\boldsymbol{M}^{\mathrm{tg},b}[k]] + \underline{B}^b[k]), \tag{23}$$

where the block tangent modulus $\boldsymbol{M}^{\mathrm{tg},b}[k] = \mathrm{diag}(\boldsymbol{M}^{\mathrm{tg},l_1}, \ldots, \boldsymbol{M}^{\mathrm{tg},l_p})$.

The problem of eliminating the incompatibility $e^b[k]$ is equivalent to minimizing the scalar function $f(\underline{\Sigma}) = \|\underline{F}^b[k^*]\|^2/2$ that is solved here using the trust region method (Conn et al., 1987, Kelley, 1999). Each step of the process involves approximating the local variation of $f(\underline{\Sigma})$ around the current iterate $\underline{\Sigma}_0$ by the quadratic model

$$f(\underline{\Sigma}) = f(\underline{\Sigma}_0) + (\nabla f)^T(\underline{\Sigma} - \underline{\Sigma}_0) + (\underline{\Sigma} - \underline{\Sigma}_0)^T\nabla^2 f(\underline{\Sigma} - \underline{\Sigma}_0)/2, \tag{24}$$

where the gradient $\nabla f = \underline{J}^b[k]\underline{F}^b[k]$, and Hessian $\nabla^2 f = (\underline{J}^b[k])^T\underline{J}^b[k]$. The predicted reduction in $f(\underline{\Sigma})$ is given by

$$\hat{\Delta} = -(\nabla f)^T(\underline{\Sigma} - \underline{\Sigma}_0) - (\underline{\Sigma} - \underline{\Sigma}_0)^T\nabla^2 f(\underline{\Sigma} - \underline{\Sigma}_0)/2. \tag{25}$$

Note that the size of the optimization problem grows exponentially with b.

2.4.7 Stress increment partitioning

We now give a formula for partitioning a given stress perturbation $\delta\boldsymbol{\sigma}^{[k]}$ imposed at node k among its children subject to the constraints

$$\begin{aligned} \rho^{[k]}[\delta\boldsymbol{\sigma}^{[l(k)]}] + (1-\rho^{[k]})[\delta\boldsymbol{\sigma}^{[r(k)]}] &= [\delta\boldsymbol{\sigma}^{[k]}], \text{ and,} \\ \underline{P\alpha}^{[k]}[\delta[\![\dot{\boldsymbol{\epsilon}}^{[k]}]\!]] + \underline{Q\alpha}^{[k]}[\delta[\![\boldsymbol{\sigma}^{[k]}]\!]] &= \mathbf{0}. \end{aligned} \tag{26}$$

The first condition above demands preservation of the average property in Eq. (2a), and the second condition demands maintenance of the current state

of incompatibility between the child nodes of k. Noting that $\delta\dot{\boldsymbol{\epsilon}}^{[l(k)]} = \boldsymbol{M}^{\mathrm{tg}}[l(k)]\delta\boldsymbol{\sigma}^{[l(k)]}$, and $\delta\dot{\boldsymbol{\epsilon}}^{[r(k)]} = \boldsymbol{M}^{\mathrm{tg}}[r(k)]\delta\boldsymbol{\sigma}^{[r(k)]}$, we get $\delta\boldsymbol{\sigma}^{l(k)} = \boldsymbol{A}^{[k]}\delta\boldsymbol{\sigma}^{l(k)}$, where $\boldsymbol{A}^{[k]}$ is given by Eq. (19), and

$$\begin{aligned}\delta\boldsymbol{\sigma}^{[l(k)]} &= (\rho^{[k]}\boldsymbol{I} + (1-\rho^{[k]})\boldsymbol{A}^{[k]})^{-1}\delta\boldsymbol{\sigma}^{[k]},\\ \delta\boldsymbol{\sigma}^{[r(k)]} &= (\rho^{[k]}\boldsymbol{A}^{[k]} + (1-\rho^{[k]})\boldsymbol{I})^{-1}\delta\boldsymbol{\sigma}^{[k]}.\end{aligned} \tag{27}$$

2.4.8 Solution algorithm

The trust region (Conn et al., 1987, Kelley, 1999) based solution algorithm is given in Alg. 1. It involves iteratively lowering the $e^b[k^*]$ of node k^* with the largest incompatibility error, using a local quadratic model of the incompatibility surface near the present state of stress.

3 Numerical results

In this section, we present the results of numerical simulations of deformation of a copper polycrystal comprising of $N_g = 256$ initially randomly oriented grains of equal volume comprising the leaves of a hierarchical model described above. All simulations start with the same set of uniformly distributed random interfacial normals $\boldsymbol{\nu}^{[k]}$ between sibling nodes of the hierarchy. The polycrystal is represented as a balanced binary tree with $N_n = 511$ nodes. Node $r = 511$ is the root of the tree with height $h[r] = 9$.

We begin by fitting the parameters of the hardening model of Sec. 2.3 to the experimental data of Tomé et al. (1984) under monotonic tension, compression, and torsion of copper. Fitting is done to both the hierarchical and VPSC models. In the hierarchical model, tension, and compression are imposed using the relaxed constraints on the root node $r = 511$, whereas torsion is imposed using full constraints. All three loadings are imposed using full constraints in the VPSC model. Comparison of the experimental and model generated stress-strain response for both the hierarchical and VPSC models are shown in Fig. 2. The extended Voce hardening parameters used in fitting are given in Table 1.

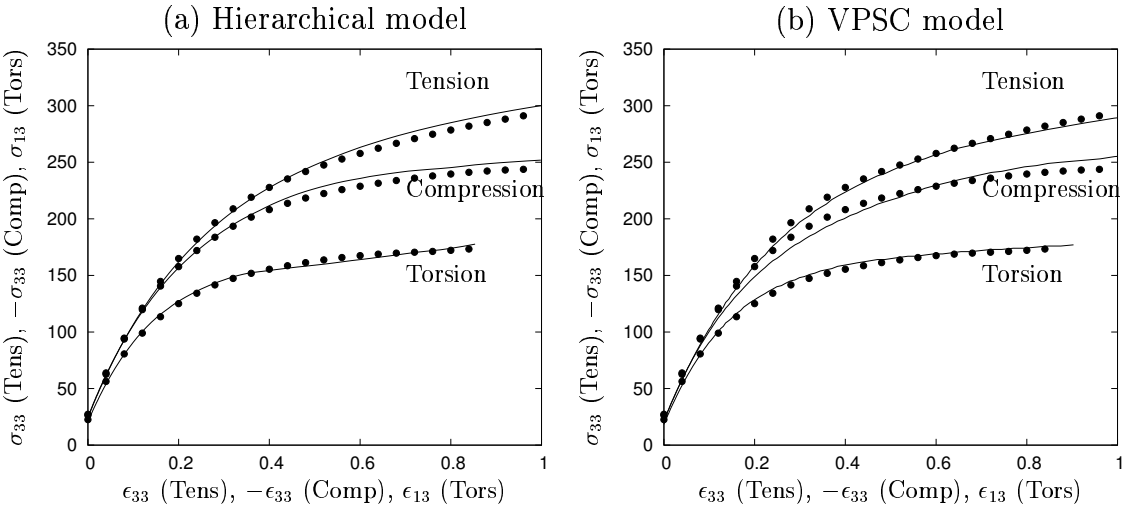

Fig. 2. Comparison of the experimental data of Tomé et al. (1984), indicated by dots, with that of a 256 grain hierarchical model (a), and VPSC calculation (b), indicated by continuous lines. The fitting parameters are listed in Table 1.

It is seen from Fig. 2 that both the hierarchical model, and the self-consistent model succeed in fitting the experimental data. Whereas the parameters needed to fit the tension and compression curves using the hierarchical model are com-

Table 1

Voce parameters (in MPa) used in fitting Tomé et al. (1984)'s experimental stress strain curves using the hierarchical and VPSC models. The latent hardening constants are $h_0 = 1$, $h_1 = 1.2$, $h_2 = 1.25$, and $h_3 = 1.3$.

	Hierarchical model				VPSC model			
Loading	τ_0	θ_0	τ_1	θ_1	τ_0	θ_0	τ_1	θ_1
Tension	15	190	110	4	12	280	150	10
Compression	15	190	110	1	12	290	135	1
Torsion	15	120	66	9	12	280	110	10

parable (the only small difference being in θ_1), they are markedly different from those needed to fit the torsion curve. The parameters needed for fitting all three curves are different for the VPSC model.

The difficulty of finding a common set of Voce parameters for all loading paths was noted by Tomé et al. (1984). In fitting their data with a full constraints model, and with a model that transitions from full to relaxed constraints as grains become flatter, they found that accounting for texture evolution can only partially explain the different stress-strain response along different loading paths. They argued that the rest of the discrepancy is caused by loading-path dependent sub-structure formation and hardening of grains, and that different Voce parameters are needed to account for distinct sub-structures. Direct experimental evidence demonstrating that the sub-structure pattern in tension, and in torsion are different was given by Bassim and Liu (1993) for commercial copper, and likely arises because grains rotate toward well defined stable orientations during uniaxial tension but undergo constant rotation and

do not approach stable orientations (Kocks et al., 1998, Chap. 5, Sec. 1.3) during torsional deformation. The extended Voce law of Eq. (10) is unable to capture the hardening patterns under both schemes of sub-structure evolution. This necessitates significantly different parameters to fit tension and compression on the one hand and torsion on the other.

The Voce parameters used to fit the tension and compression curves using the hierarchical model are much closer to each other than those obtained by fitting these same curves with the VPSC model. We interpret this to physically mean that whereas the hierarchical model succeeds in fitting both curves by assuming similar average sub-structural evolution within grains, the VPSC model requires an assumption of different sub-structural evolution. In view of the rotation pattern of grains toward stable orientations in both tension and compression, the hypothesis of similar sub-structural evolution in both tension and compression, as given by the hierarchical model, appears more reasonable.

3.2 Plane strain deformation of copper polycrystals

We now analyze in detail the plane strain deformation of a hierarchical copper polycrystal to a rolling reduction of 74%. Because grains rotate toward well defined stable orientations during rolling, we assume the hardening parameters fit to the tension data from Table 1, which are similar to those that fit the compression data. Plane strain boundary conditions are imposed either on the entire hierarchy at node 511, which is the only element of the set $\mathscr{H}^9$, or on the 16 sub-hierarchies rooted at the nodes comprising $\mathscr{H}^5$, or on the 256 sub-hierarchies rooted at the nodes comprising $\mathscr{H}^1$. $\mathscr{H}^1$ loading is equivalent to

the Taylor model, and will serve as a point of comparison for the other results. Both full (FC) and relaxed constraints (RC) are imposed. We distinguish between the *trivial* hierarchical models ($\mathscr{H}^1$ FC and RC models) and the *true* hierarchical models ($\mathscr{H}^5$ and $\mathscr{H}^9$ FC and RC models) below. Also, $\epsilon_{\rm vM} = \int_0^t \sqrt{(2/3)\dot{\boldsymbol{\epsilon}}^{[r]}(\tau) : \dot{\boldsymbol{\epsilon}}^{[r]}(\tau)} d\tau$ denotes the von Mises strain at the root node of the hierarchy, and RD, TD, and ND respectively denote the rolling, transverse and normal directions.

Figure 3 shows the calculated {111} pole figures after 74% reduction for different constraints, and for different sets chosen for constraint imposition. Four fold symmetrization of the pole figures is done for easy comparison with the experimentally measured pole figure of Hirsch and Lucke (1988a). Similarly, the choice of the displayed set of level lines overlaps that of Hirsch and Lucke (1988a). The peak intensity in the simulated {111} pole figures corresponding to FC on $\mathscr{H}^9$ (Fig. 3a), FC on $\mathscr{H}^5$ (Fig. 3b), and RC on $\mathscr{H}^9$ (Fig. 3d), are 5.6, 6.4, and 6.3, respectively, and agree well with the peak experimental intensity of 6.0. Thus, all the true hierarchical models fit the peak experimental stress intensity well. Their pole figures are also in good qualitative agreement with the experimental pole figure of Hirsch and Lucke (1988a). Trivial hierarchical FC and RC calculations however result in more than double the experimental peak intensity being predicted (Fig. 3c and Fig. 3e). This agrees with the well known (Hirsch and Lucke, 1988b, Butler and McDowell, 1998, Lebensohn, 2001) tendency of the Taylor model to overestimate the texturing rate. Fig. 3f shows the final texture predicted by a viscoplastic self-consistent (VPSC) calculation (Lebensohn and Tomé, 1993). The predicted peak intensity is intermediate between that of the trivial and true hierarchical models.

The underlying reason for the markedly different peak intensities of the $\mathscr{H}^9$

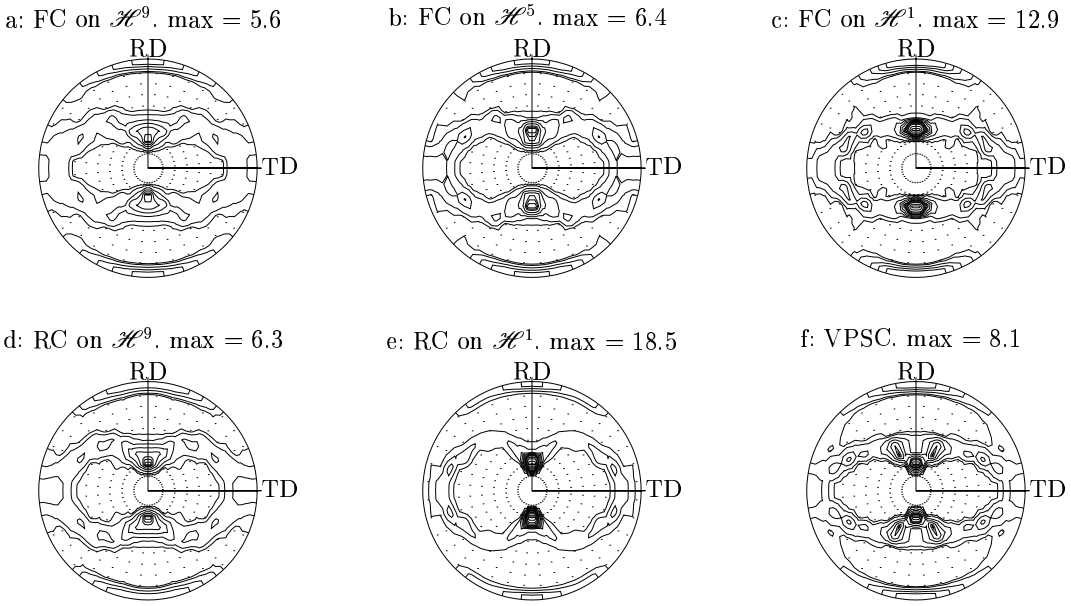

Fig. 3. Calculated {111} pole figures after a rolling reduction of 74% from 256-grain simulations using the hierarchical polycrystal model (a-e), and using the viscoplastic self consistent model (Lebensohn and Tomé, 1993) (f). Four-fold symmetrization of the pole figures and the choice of the level lines (0.5, 1, 2, 3, 4, 5, 5.5, 6, 7, 8, 10, 12, 15, and 18) correspond to the experimental pole figure of Hirsch and Lucke (1988a).

and $\mathscr{H}^1$ FC models is seen by comparing the distribution of grain lattice spin axes (the dual of $\boldsymbol{W}_{\text{lat}}^{[k]}$) in Fig. 4. It is seen that the dominant direction of the lattice spin axes moves from close to TD in the early stages of deformation to lie on the RD–ND plane with increasing deformation, for both FC on $\mathscr{H}^9$ and FC on $\mathscr{H}^1$, but is less clustered in these regions under $\mathscr{H}^9$ constraints than under $\mathscr{H}^1$ constraints. Taken together with the observation that the mean grain spin rates for the $\mathscr{H}^9$ model are higher (0.67 at $\epsilon_{\text{vM}} = 0.25$ and 0.26 at $\epsilon_{\text{vM}} = 1.35$) than those for the $\mathscr{H}^1$ model (0.49 at $\epsilon_{\text{vM}} = 0.25$ and 0.18 at $\epsilon_{\text{vM}} = 1.35$), we conclude that the reduced peak intensity in Fig. 3a compared to Fig. 3c originates from the greater scattering of the lattice spin axes of the grains in the $\mathscr{H}^9$ model, and not because of smaller lattice spin magnitudes

in the $\mathscr{H}^9$ model.

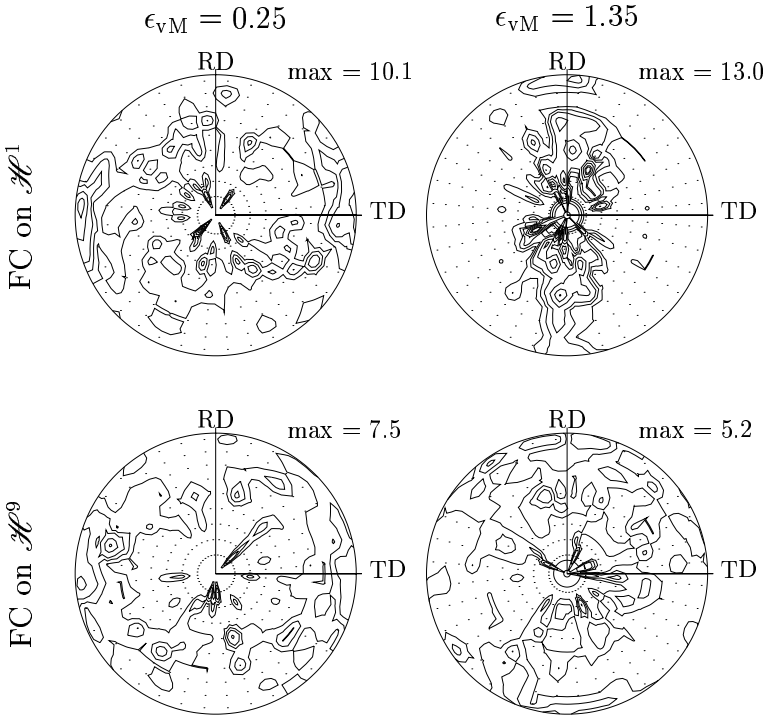

Fig. 4. Pole figure representation of the lattice spin axis at $\epsilon_{\mathrm{vM}} = 0.25$ (first column), and at $\epsilon_{\mathrm{vM}} = 1.35$ (second column) for FC at $\mathscr{H}^1$ (first row), and FC at $\mathscr{H}^9$ (second row). The plotted levels are 1, 2, 3, 5, 7, 9, 10, and 13.

The continuity conditions demanded in the hierarchical model affects the activation of slip systems in individual grains. Following Lebensohn and Tomé (1993), we take a slip system to be active in a grain if its absolute slip rate is at least 5% of the maximum absolute slip rate in that grain. Fig. 5 shows the evolution with deformation of $\langle N_{\mathrm{act}} \rangle$, the average number of active slip systems. It is seen that (i) the four true hierarchical models exhibit similar evolution (Fig. 5b), which suggests that the continuity conditions between nodes of small height determine the grain fields, and (ii) all the true hierarchical models result in greater activity than the VPSC model, which suggests that the condition of deformation compatibility with neighboring grains imposes greater constraint on the grains than the condition of deformation compatibil-

ity with a homogeneous effective medium as in the VPSC model. The greater constraint imposed on each grain in the Taylor FC ($\mathscr{H}^1$) model also explains its much larger $\langle N_{\rm act}\rangle$ compared to all the other models. (iii) The $\langle N_{\rm act}\rangle$ of the true hierarchical models, the Taylor RC model, and the VPSC model become similar with increasing deformation.

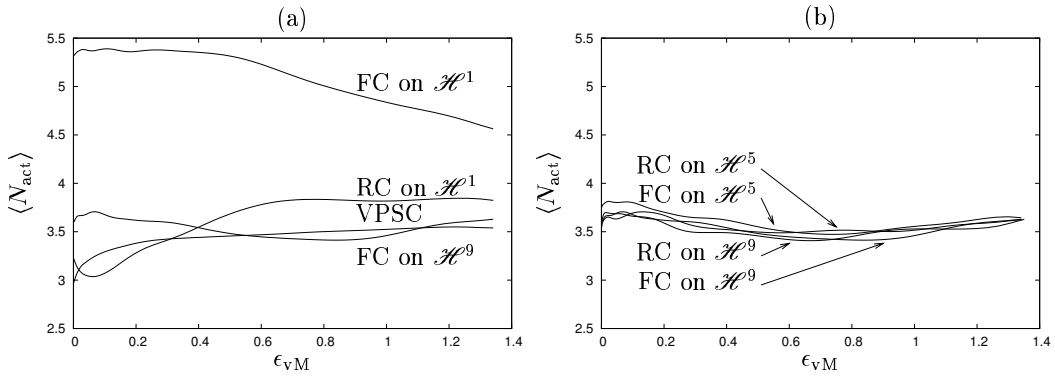

Fig. 5. Evolution of the average number of active slip systems, $\langle N_{\rm act}\rangle$ in the grains calculated by various models. (a) Evolution for three mean field models and one true hierarchical model (FC on $\mathscr{H}^9$), and (b) Comparison of the different true hierarchical models.

Another measure of the division of the imposed deformation among the grains is obtained by considering the average deviation of the deformation of grains from plane strain, given that the macroscopically imposed deformation is plane strain. We quantify planarity of grain deformation using the intermediate eigenvalue of the strain rate tensor, i.e., if $\lambda_1^{[k]} \leq \lambda_2^{[k]} \leq \lambda_3^{[k]}$ are the eigenvalues of $\dot{\boldsymbol{\epsilon}}^{[k]}$, $k \in \mathscr{L}$, Fig. 6 plots the evolution of the standard deviation of λ_2 with deformation. Again, we observe that (i) all the true hierarchical models have similar $\langle\lambda_2^2\rangle^{\frac{1}{2}}$ evolution with imposed deformation, and these show considerable non-planarity of deformation that however, decreases with deformation. (ii) At the early stages of the deformation, the VPSC model coincides with the Taylor RC model (RC on $\mathscr{H}^1$), but transitions toward the true hier-

archical models with increasing deformation. (iii) Of all the models, the Taylor RC model shows the least deviation from planarity.

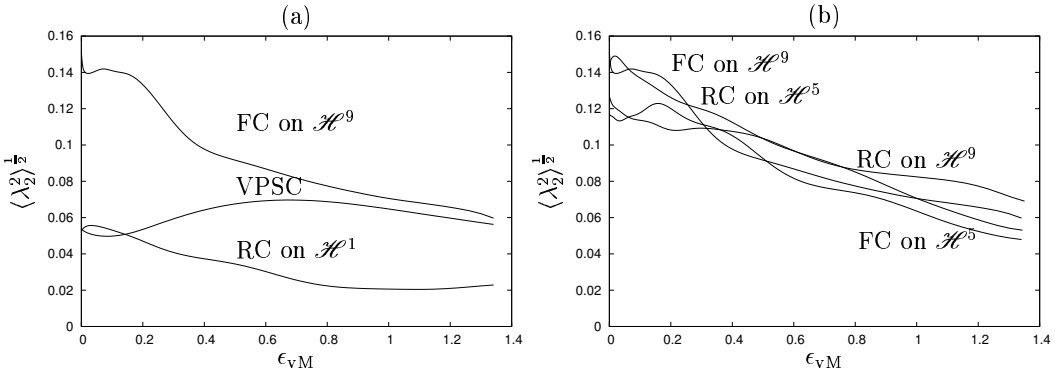

Fig. 6. Evolution of the deviation of average grain deformation from plane strain deformation. (a) Evolution for two mean field models and one true hierarchical model (FC on $\mathscr{H}^9$), and (b) Comparison of the different true hierarchical models. Note that $\langle\lambda_2^2\rangle^{\frac{1}{2}} \equiv 0$ for FC on $\mathscr{H}^1$.

A measure of the constraint experienced by individual grains constituting the polycrystal is the deviation of the granular strain rate, $\dot{\boldsymbol{\epsilon}}^{[k]}$ and stress $\boldsymbol{\sigma}^{[k]}$, $k \in \mathscr{L}$, from $\dot{\boldsymbol{\epsilon}}^{[r]}, \boldsymbol{\sigma}^{[r]}$, where r is the root of the hierarchy. Four measures of deviation

$$
\begin{aligned}
\delta^d_{\dot{\boldsymbol{\epsilon}}} &= \left\langle \left(1 - \frac{\dot{\boldsymbol{\epsilon}}^{[k]}}{\|\dot{\boldsymbol{\epsilon}}^{[k]}\|} : \frac{\dot{\boldsymbol{\epsilon}}^{[r]}}{\|\dot{\boldsymbol{\epsilon}}^{[r]}\|} \right)^2 \right\rangle^{\frac{1}{2}}, \\
\delta^m_{\dot{\boldsymbol{\epsilon}}} &= \frac{\langle \|\dot{\boldsymbol{\epsilon}}^{[k]} - \dot{\boldsymbol{\epsilon}}^{[r]}\|^2 \rangle^{\frac{1}{2}}}{\|\dot{\boldsymbol{\epsilon}}^{[r]}\|}, \\
\delta^d_{\boldsymbol{\sigma}} &= \left\langle \left(1 - \frac{\boldsymbol{\sigma}^{[k]}}{\|\boldsymbol{\sigma}^{[k]}\|} : \frac{\boldsymbol{\sigma}^{[r]}}{\|\boldsymbol{\sigma}^{[r]}\|} \right)^2 \right\rangle^{\frac{1}{2}}, \\
\delta^m_{\boldsymbol{\sigma}} &= \frac{\langle \|\boldsymbol{\sigma}^{[k]} - \boldsymbol{\sigma}^{[r]}\|^2 \rangle^{\frac{1}{2}}}{\|\boldsymbol{\sigma}^{[r]}\|},
\end{aligned}
\tag{28}
$$

evaluated at $\epsilon_{\mathrm{vM}} = 0.25$ and $\epsilon_{\mathrm{vM}} = 1.35$ are shown in Table 2. These quantify the standard deviation of the direction ($\delta^d_{\dot{\boldsymbol{\epsilon}}}$, $\delta^d_{\boldsymbol{\sigma}}$) and magnitude ($\delta^m_{\dot{\boldsymbol{\epsilon}}}$, $\delta^m_{\boldsymbol{\sigma}}$) differences between the grain fields ($\dot{\boldsymbol{\epsilon}}^{[k]}$, $\boldsymbol{\sigma}^{[k]}$), $k \in \mathscr{L}$ from their macroscopic averages ($\dot{\boldsymbol{\epsilon}}^{[r]}$, $\boldsymbol{\sigma}^{[r]}$). We observe that: (i) Each of $\delta^d_{\dot{\boldsymbol{\epsilon}}}$, $\delta^d_{\boldsymbol{\sigma}}$, $\delta^m_{\dot{\boldsymbol{\epsilon}}}$, and $\delta^m_{\boldsymbol{\sigma}}$ is com-

Table 2

Deviation of the grain fields $(\dot{\boldsymbol{\epsilon}}^{[k]}, \boldsymbol{\sigma}^{[k]})$, $k \in \mathscr{L}$ from the macroscopic averages $(\dot{\boldsymbol{\epsilon}}^{[r]}, \boldsymbol{\sigma}^{[r]})$ after 29% and 74% rolling reduction.

Loading	$\epsilon_{\mathrm{vM}} = 0.25$				$\epsilon_{\mathrm{vM}} = 1.35$			
	$\delta^d_{\dot{\boldsymbol{\epsilon}}}$	$\delta^m_{\dot{\boldsymbol{\epsilon}}}$	$\delta^d_{\boldsymbol{\sigma}}$	$\delta^m_{\boldsymbol{\sigma}}$	$\delta^d_{\dot{\boldsymbol{\epsilon}}}$	$\delta^m_{\dot{\boldsymbol{\epsilon}}}$	$\delta^d_{\boldsymbol{\sigma}}$	$\delta^m_{\boldsymbol{\sigma}}$
$\mathscr{H}^1$ FC	0.000	0.000	0.200	0.327	0.000	0.000	0.156	0.198
$\mathscr{H}^5$ FC	0.094	0.286	0.161	0.263	0.131	0.274	0.129	0.214
$\mathscr{H}^9$ FC	0.109	0.356	0.146	0.261	0.137	0.291	0.128	0.217
$\mathscr{H}^1$ RC	0.097	0.119	0.161	0.323	0.133	0.169	0.153	0.220
$\mathscr{H}^5$ RC	0.101	0.298	0.154	0.266	0.139	0.229	0.131	0.225
$\mathscr{H}^9$ RC	0.119	0.347	0.155	0.270	0.154	0.266	0.132	0.214
VPSC	0.061	0.234	0.024	0.133	0.086	0.087	0.046	0.161

parable for all the true hierarchical models at both low and high ϵ_{vM}. This reinforces our earlier suggestion that the continuity conditions imposed between nodes of small height determine the scatter of the $\dot{\boldsymbol{\epsilon}}^{[k]}$, and $\boldsymbol{\sigma}^{[k]}$, $k \in \mathscr{L}$ fields. (ii) Compared to the true hierarchical models, the VPSC model results in much smaller scatter of the grain fields (both strain rate and stress) from that of the macroscopic average, at both stages of the deformation process considered. (iii) $\delta^d_{\boldsymbol{\sigma}}$, and $\delta^m_{\boldsymbol{\sigma}}$ for the true hierarchical models are comparable to that of Taylor RC model ($\mathscr{H}^1$ RC). This is not true for $\delta^d_{\dot{\boldsymbol{\epsilon}}}$, and $\delta^m_{\dot{\boldsymbol{\epsilon}}}$.

The computer run time of the different models, normalized against the run time of FC loading on $\mathscr{H}^1$ are 0.83 (FC on $\mathscr{H}^5$), 1.83 (FC on $\mathscr{H}^9$), 1.40 (RC on $\mathscr{H}^1$), 0.68 (RC on $\mathscr{H}^5$), and 1.92 (RC on $\mathscr{H}^9$). Throughout, we have taken $b = 9$ (Sec. 2.4.5). Surprisingly, the $\mathscr{H}^5$ calculations are faster than the corresponding $\mathscr{H}^1$ calculations, although, the $\mathscr{H}^9$ calculations are more time consuming than the $\mathscr{H}^1$ calculations. This is because the total computational time is the product of the time to set up and solve the quadratic incompatibility problem (Sec. 2.4.6), and the number of such problems. $\mathscr{H}^5$ calculations turn out to be faster than $\mathscr{H}^1$ calculations because the simultaneous correction of the stresses in 16 grains arrives at a compatible system of fields with fewer steps, even though each set of the solution is more time consuming. In $\mathscr{H}^9$ calculations however, the solution time of the much larger quadratic model is large enough to outweigh the reduction in the number of solution steps.

We reemphasize that all the true hierarchical calculations involve the same order of magnitude of computational effort as a Taylor ($\mathscr{H}^1$) calculation, unlike a full crystallographic finite element or N-site calculation, which typically is at least two orders more computationally intensive than any of the mean field models.

4 Discussion

In Sec. 3.2, four measures of grain response in hierarchical polycrystals were considered: the texture evolution, activity of slip systems, planarity of grain

deformation, and statistical deviations of the grain stress and strain-rate fields from the macroscopic average. In every measure considered, the true hierarchical models showed similar response regardless of the imposed constraint (FC or RC) and regardless of the node set for constraint imposition ($\mathscr{H}^5$ or $\mathscr{H}^9$). This suggests that the requirement of compatibility and traction continuity (Eq. (3)) between children of the more numerous nodes of small height statistically dominates that between children of the fewer nodes of larger height in determining the granular fields. In other words, it appears that truncation of the hierarchy beyond a certain height (≈ 5 for copper) has little deleterious influence upon the statistics of the computed grain response in the hierarchical model. The optimal height for truncation will depend upon the anisotropy of the crystal response, with more anisotropic crystals requiring truncation at greater heights to fully capture the statistics of their response. This leads us to suggest that a computationally light model of a polycrystal that accounts for intergranular interactions would comprise of a mean field model like the Taylor or the VPSC model wherein the grains are replaced by binary trees of small height. The $\mathscr{H}^5$ models are examples of such hybrid models of the polycrystal. Indeed, it has been shown that these calculations are computationally lighter still than their respective Taylor calculations.

It was stated in Sec. 1 that the binary tree model cannot capture intergranular interactions to the same level of detail as a true microstructural model (Kalidindi et al., 1992, Lebensohn, 2001). Topologically, this derives from the absence of closed loop paths through the leaves (grains) of the binary tree, unlike in the actual microstructure. However, it is precisely the absence of closed loops in the binary tree model that enables its rapid solution, as the solution of sub-hierarchies can be accomplished without consideration of the

rest of the hierarchy.

We now discuss the construction of the binary tree model from given microstructural information from say, a 2D micrograph. A single step in this process involves dividing a region (represented by node k) of the micrograph into two sub-regions ($l(k)$ and $r(k)$), according to the criterion below. The process can be recursively applied to each of the two sub-regions to obtain further sub-division. Desirable properties of the dividing curve between the two sub-regions are that it must (i) be a continuous union of grain boundary segments, (ii) approach planarity (linearity in 2D) as closely as possible, so that assignment of a normal vector $\boldsymbol{\nu}^{[k]}$ to this interface corresponds to physical reality, and (iii) divide the region such that $\rho^{[k]} \approx 0.5$. Each such potential dividing curve can be assigned an effective normal vector $\boldsymbol{\nu}^{[k]} = \sum_i l_i \boldsymbol{N}_i / \| \sum_i l_i \boldsymbol{N}_i \|$, where $\boldsymbol{N}_i$ represents the unit normal of the i-th segment of the contour, of length l_i and the optimal dividing curve defined as one that minimizes the cost function

$$C = W_\rho \left(\rho^{[k]} - \frac{1}{2} \right)^2 + W_{\boldsymbol{n}} \left(\frac{\sum_i l_i (\boldsymbol{N}_i \cdot \boldsymbol{\nu}^{[k]})^2}{\sum_i l_i} - 1 \right)^2 , \tag{29}$$

where $W_\rho + W_{\boldsymbol{n}} = 1$. An attempt to implement this procedure on actual microstructures to compute the grain fields is deferred to future work.

5 Conclusion

A hierarchical model of a rate-dependent polycrystal that explicitly accounts for inter-granular interactions, and is yet comparable in computational effort to mean field models is proposed, and an algorithm for its solution is given. Deformation along various monotonic loading paths of a copper polycrystal

have been analyzed using this model under different constraints. Good agreement with experimental observations is found. Further, it is found that all the true hierarchical models tested lead to similar macroscopic response, suggesting that the continuity conditions applicable near the lowest level of the binary tree dominate the determination of granular deformation.

It is therefore suggested that computationally efficient modeling of a polycrystal while accounting for the interaction between grains can be accomplished by embedding short binary trees (of height approximately 5 in f.c.c. copper) in the place of grains in conventional mean field models.

Acknowledgments: The author gratefully acknowledges use of the `POLE` software developed by Dr. Carlos Tomé (Los Alamos National Laboratory) for plotting the pole figures shown here, and the `VPSC` software developed by Dr. Ricardo Lebensohn (Los Alamos National Laboratory) and Dr. Carlos Tomé for generating all the results concerning the VPSC model (Lebensohn and Tomé, 1993). The author also thanks Prof. Bharath Rangarajan (University of Minnesota) for his helpful suggestions on optimization algorithms.

References

Asaro, R. J., Needleman, A., 1985. Overview 42. Texture development and strain-hardening in rate dependent polycrystals. Acta metall. 33 (6), 923–953.

Barnett, M. R., Nave, M. D., Bettles, C. J., 2004. Deformation microstructures and textures of some cold rolled Mg alloys. Mater. Sci. Eng. A 386 (1-2), 205–211.

Bassim, M. N., Liu, C. D., 1993. Dislocation cell structures in copper in torsion and tension. Mat. Sci. Eng. A A164, 170–174.

Beyerlein, I. J., Tomé, C. N., 2008. A dislocation-based constitutive law for pure zr including temperature effects. Int. J. Plasticity 24 (5), 727–745.

Buchheit, T. E., Wellman, G. W., Battaile, C. B., 2005. Investigating the limits of polycrystal plasticity modeling. Int. J. Plasticity 21 (2), 221–249.

Butler, G. C., McDowell, D. L., 1998. Polycrystal constraint and grain subdivision. Int. J. Plasticity 14 (8), 703–717.

Canova, G. R., Fressengeas, C., Molinari, A., Kocks, U. F., 1988. Effect of rate sensitivity on slip system activity and lattice rotation. Acta Metall. 38 (8), 1961–1970.

Conn, A. R., Gould, G. I. M., Toint, P. L., 1987. Trust-region methods. SIAM.

Cormen, T. H., Leiserson, C. E., Rivest, R. L., 1990. Introduction to Algorithms. MIT press, Cambridge.

Dillamore, I. L., Katoh, H., 1974. A comparison of the observed and predicted deformation textures in cubic metals. Metal Sci. 8, 21–27.

Duchêne, L., El Houdaigui, F., Habrake, A. M., 2007. Length changes and texture prediction during free end torsion test of copper bars with FEM and remeshing techniques. Int. J. Plasticity 23 (8), 1417–1438.

Franciosi, P., Zaoui, A., 1982. Multislip in FCC crystals: A theoretical approach compared with experimental data. Acta metall. 30, 1627–1637.

Gan, Y. X., Wei, C. S., Lam, M., Wei, X., Lee, D., Kysar, J. W., Chen, X., 2007. Deformation and fracture behavior of electrocodeposited alumina nanoparticle/copper composite films. J. Mater Sci 42 (13), 5256–5263.

Grujicic, M., Cao, G., Batchu, S., 2003. Crystal plasticity-based finite element analysis of deformation and fracture of polycrystalline lamellar γ-TiAl + α-Ti_3Al alloys. J. Mater. Sci. 38 (2), 307–322.

Guan, Y., Pourboghrat, F., Barlat, F., 2006. Finite element modeling of tube hydroforming of polycrystalline aluminum alloy extrusions. Int. J. Plasticity 22 (12), 2366–2393.

Héripré, E., Dexet, M., Crépin, J., L. Gélébart, A. R., Bornert, M., Caldemaison, D., 2007. Coupling between experimental measurements and polycrystal finite element calculations for micromechanical study of metallic materials. Int. J. Plasticity 23 (9), 1512–1539.

Hill, R., 1961. Discontinuity relations in mechanics of solids. In: Sneddon, I. N., Hill, R. (Eds.), Progress in Solid Mechanics. Vol. 2. Interscience Publishers, New York, Ch. 6, pp. 247–278.

Hill, R., 1965. Continuum micro-mechanics of elastoplastic polycrystals. J. Mech. Phys. Solids 13, 89–101.

Hirsch, J., Lucke, K., 1988a. Mechanism of deformation and development of rolling textures in polycrystalline FCC metals: I Description of rolling texture in homogeneous cuzn alloys. Acta metall. 36 (11), 2863–2882.

Hirsch, J., Lucke, K., 1988b. Mechanism of deformation and development of rolling textures in polycrystalline FCC metals: II Simulation and interpretation of experiments on the basis of Taylor-type theories. Acta metall. 36 (11), 2883–2904.

Honeff, H., Mecking, H., 1978. Icotom 5. In: Proc. 5th Int. Conf. on the Textures of Materials. Vol. 1. Springer-Verlag, pp. 265–275.

Hughes, D. A., Liu, Q., Chrzan, D. C., Hansen, N., 1997. Scaling of microstructural parameters: Misorientations of deformation induced boundaries. Acta mater. 45 (1), 105–112.

Kalidindi, S. R., Bronkhorst, C. A., Anand, L., 1992. Crystallographic texture evolution in bulk deformation processing of FCC metals. J. Mech. Phys. Solids, 537–569.

Kelley, C. T., 1999. Iterative Methods for Optimization. No. 18 in Frontiers in Applied Mathematics. SIAM, Philadelphia.

Knezevic, M., Kalidindi, S. R., Fullwood, D., 2008. Computationally efficient database and spectral interpolation for fully plastic Taylor-type crystal plasticity calculations of face-centered cubic polycrystals. Int. J. Plasticity ..., doi:10.1016/j.ijplas.2007.12.002.

Kocks, U. F., Tomé, C. N., Wenk, H. R., 1998. Texture and Anisotropy. Cambridge University Press, Cambridge, U.K.

Lebensohn, R., 1999. Modeling the role of local correlations in polycrystal plasticity using viscoplastic self-consistent schemes. Modeling Simul. Mater. Sci. Eng. 7, 739–746.

Lebensohn, R. A., 2001. N-Site modeling of a 3D viscoplastic polycrystal using fast fourier transform. Acta mater 49, 2723–2737.

Lebensohn, R. A., Turner, P. A., Signorelli, J. W., Canova, G. R., Tomé, C. N., 1998. Calculation of intergranual stresses based on a large strain visoplastic self-consistent polycrystal model. Modelling Simul. Mater. Sci. Eng. 6, 447–465.

Lebensohn, R. E., Tomé, C. N., 1993. A self-consistent anisotropic approach for the simulation of plastic deformation and texture development of polycrystals: application to zirconium alloys. Acta metall. mater 41 (9), 2611–2624.

Lee, D., Wei, X., Zhao, M., Chen, X., Jun, S. C., Hone, J., Kysar, J. W., 2007. Plastic deformation in nanoscale gold single crystals and open-celled nanoporous gold. Modelling Simul. Mater. Sci. Eng. 15 (1), 181–192.

Leffers, T., Christoffersen, H., 1997. The importance of grain-to-grain interaction during rolling deformation of copper. Mater. Sci. Eng. A234–236, 676–679.

Lin, T. H., 1964. Slip and stress fields of a polycrystalline aggregate at different

stages of loading. J. Mech. Phys. Solids 12, 391–408.

Mahesh, S., 2005. Deformation banding and shear banding in single crystals. Acta mater. 54 (17), 4565–4574.

Mahesh, S., Tomé, C. N., 2004. Deformation banding under arbitrary monotonic loading in cubic metals. Phil. Mag. 84, 3517–3546.

Mahesh, S., Tomé, C. N., McCabe, R. J., Kaschner, G. C., Beyerlein, I. J., Misra, A., 2004. Application of a sub-structure based hardening model to copper under loading path changes. Metall Mater Trans A 35, 3763–3774.

Manonukul, A., Dunne, F. P. E., 2004. High- and low-cycle fatigue crack initiation using polycrystal plasticity. Proc. R. Soc. A 460 (2047), 1881–1903.

Mayeur, J. R., McDowell, D. L., 2007. A three-dimensional crystal plasticity model for duplex Ti-6Al-4V. Int. J. Plasticity 23 (9), 1457–1485.

Molinari, A., Canova, G. R., Ahzi, S., 1987. A self consistent approach of the large deformation polycrystal viscoplasticity. Acta metall. 35, 2983–2994.

Nemat-Nasser, S., Maximenko, A., Olevsky, E., 2006. Modeling the plastic response of thin metal membranes. J. Mech. Phys. Solids 54 (11), 2474–2494.

Ortiz, M., Repetto, E. A., 1999. Nonconvex energy minimization and dislocation structures in ductile single crystals. J. Mech. Phys. Solids 47, 397–462.

Ortiz, M., Repetto, E. A., Stainier, L., 2000. A theory of subgrain dislocation structures. J. Mech. Phys. Solids 48, 2077–2114.

Paul, H., Driver, J. H., Maurice, C., Piatkowski, A., 2007. The role of shear banding on deformation texture in low stacking fault energy metals as characterized by model Ag crystals. Acta mater. 55, 575–588.

Peeters, B., Seefeldt, M., Teodosiu, C., Kalidindi, S. R., Houtte, P. V., Aernoudt, E., 2001a. Work-hardening/softening behavior of bcc polycrystals during changing strain paths: I An integrated model based on substructure

and texture evolution, and its prediction of the stress-strain behavior of an IF steel during two-stage strain paths. Acta Mater. 49, 1607–1619.

Peeters, B., Bacroix, B., Teodosiu, C., Houtte, P. V., Aernoudt, E., 2001b. Work-hardening/softening behavior of bcc polycrystals during changing strain paths: II TEM observations of dislocation sheets in an if steel during two-stage strain paths and their representation in terms of dislocation densities. Acta Mater. 49, 1621–1632.

Pierce, D., Asaro, R. J., Needleman, A., 1982. An analysis of nonuniform and localized deformation in ductile single crystals. Acta mater. 30, 1087–1119.

Powell, M. J. D., 1970. A Hybrid Method for Nonlinear Equations. Gordon and Breach, Ch. Numerical Methods for Nonlinear Algebraic Equations.

Proust, G., Tomé, C. N., Kaschner, G. C., 2007. Modeling texture, twinning and hardening evolution during deformation of hexagonal materials. Acta mater. 55, 2137–2148.

Shenoy, M., Tjiptowidjojo, Y., McDowell, D., 2008. Microstructure-sensitive modeling of polycrystalline in 100. Int. J. Plasticity ..., doi:10.1016/j.ijplas.2008.01.001.

Shiekhelsouk, M. N., Favier, V., Inal, K., Cherkaoui, M., 2008. Modelling the behaviour of polycrystalline austenitic steel with twinning-induced plasticity effect. Int. J. Plasticity ..., doi:10.1016/j.ijplas.2007.11.004.

Taylor, G. I., 1938. Plastic strain in metals. Journal of the Inst Metals 62, 307.

Thorning, C., Somers, M. A. J., Wert, J. A., 2005. Grain interaction effects in polycrystalline cu. Mater. Sci. Eng. A397 (1–2), 215–228.

Tomé, C., Canova, G. R., Kocks, U. F., Christodoulou, N., Jonas, J. J., 1984. The relation between macroscopic and microscopic strain hardening in F.C.C polycrystals. Acta metall. 32 (10), 1637–1653.

Van Houtte, P., Delannay, L., Kalidindi, S. R., 2005. Comparison of two grain

interaction models for polycrystal plasticity and deformation texture prediction. Int. J. Plasticity 18 (3), 359–377.

Van Houtte, P., Li, S., Seefeldt, M., Delannay, L., 2002. Deformation texture prediction: from the Taylor model to the advanced lamel model. Int. J. Plasticity 21 (3), 589–624.

Weng, G. J., 1987. Anisotropic hardening of single crystals and the plasticity of polycrystals. Int. J. Plasticity 3, 315–339.

Wu, P. D., Lloyd, D. J., Jain, M., Neale, K. W., Huang, Y., 2007. Effects of spatial grain orientation distribution and initial surface topography on sheet metal necking. Int. J. Plasticity 23 (6), 1084–1104.

Zamiri, A., Pourboghrat, F., Barlat, F., 2007. An effective computational algorithm for rate-independent crystal plasticity based on a single crystal yield surface with an application to tube hydroforming. Int. J. Plasticity 23 (7), 1126–1147.

Algorithm 1 Trust region solution algorithm for the hierarchical polycrystal.

Data: Root node r; binary tree descriptors $l(k)$, $r(k)$, $p(k)$; initial guesses for $\boldsymbol{\sigma}^{[k]} \neq \mathbf{0}$, and trust radii $R[k] > 0$, $\forall k \in \mathscr{D}[r]$; $b \geq 1$, and $\varepsilon > 0$.

Result: $\dot{\boldsymbol{\epsilon}}^{[k]}$ and $\boldsymbol{\sigma}^{[k]}$ fields that satisfy Eqs. (1), (3b), and (4).

1: $k^* = r$

2: **while** $e^b[k^*] > \varepsilon$ **do**

3: Let $\underline{\Sigma}_0$ be the current iterate of stress. Calculate $\underline{F}^b[k^*](\underline{\Sigma}_0)$, and $\underline{J}^b[k^*](\underline{\Sigma}_0)$ (Sec 2.4.6).

4: Compute a step $\delta\underline{\Sigma}^b[k^*]$ to minimize the quadratic model for $f(\underline{\Sigma})$ given by Eq. (24) subject to $\|\delta\underline{\Sigma}^b[k^*]\| < R[k^*]$. Obtain $\hat{\Delta}$ from Eq. (25).

5: Partition $\delta\underline{\Sigma}^b[k^*]$ recursively (Sec. 2.4.7) to determine $\delta\boldsymbol{\sigma}^{[k]}$, $k \in \mathscr{L} \cap \mathscr{D}[k^*]$

6: Update $\boldsymbol{\sigma}^{[k]} \leftarrow \boldsymbol{\sigma}^{[k]} + \delta\boldsymbol{\sigma}^{[k]}$, recompute $\dot{\boldsymbol{\epsilon}}^{[k]}$, $k \in \mathscr{L} \cap \mathscr{D}[k^*]$ using Eq. (1), and recursively update $\dot{\boldsymbol{\epsilon}}^{[k]}$ and $\boldsymbol{\sigma}^{[k]}$, $k \in \mathscr{D}[k^*]$ using Eq. (2).

7: Recompute $e^b[k^*]$, and calculate Δ, the true reduction in f.

8: **if** $\Delta/\hat{\Delta} \leq 0$ **then**

9: $R[k^*] \leftarrow R[k^*]/4$. Reject the step $\delta\underline{\Sigma}^b[k^*]$, and go to step 4.

10: **else if** $0 < \Delta/\hat{\Delta} \leq 0.25$ **then**

11: $R[k^*] \leftarrow R[k^*]/4$. Accept the step $\delta\underline{\Sigma}^b[k^*]$.

12: **else if** $0.25 < \Delta/\hat{\Delta} \leq 0.75$ **then**

13: Accept the step $\delta\underline{\Sigma}^b[k^*]$.

14: **else**

15: $R[k^*] \leftarrow 2R[k^*]$. Accept the step $\delta\underline{\Sigma}^b[k^*]$, and go to step 4 to attempt lowering $e^b[k^*]$ further.

16: **end if**

17: Update $e^b[k]$, for all nodes k.

18: $k^* = \text{argmax}_{k \in \mathscr{D}[r]}\, e^b[k]$.

19: **end while**